Humidity-resistant gas sensors based on SnO2 nanowires coated with a porous alumina nanomembrane by molecular layer deposition

Syreina Sayegh, Jae-Hyoung Lee, Dong-Hoon Yang, Matthieu Weber, Igor Iatsunskyi, Emerson Coy, Antonio Razzouk, Sang Sub Kim, Mikhael Bechelany

Humidity-Resistant Gas Sensors Based on SnO_2 Nanowires Coated with a Porous Alumina Nanomembrane by Molecular Layer Deposition

Syreina Sayegh[1,2¥], Jae-Hyoung Lee[3¥], Dong-Hoon Yang[3], Matthieu Weber[1], Igor Iatsunskyi[4], Emerson Coy[4], Antonio Razzouk[2], Sang Sub Kim[3]*, Mikhael Bechelany[1]*

1 *Institut Européen des Membranes, IEM – UMR 5635, Univ Montpellier, ENSCM, CNRS, Montpellier, France*

2 *Laboratoire d'Analyses Chimiques, LAC – Lebanese University, Faculty of Sciences, Jdeidet 90656, Lebanon*

3 *Department of Materials Science and Engineering, Inha University, Incheon 22212, Republic of Korea.*

4 *NanoBioMedical Centre, Adam Mickiewicz University, Wszechnicy Piastowskiej 3, 61-614 Poznan, Poland*

*Corresponding authors: mikhael.bechelany@umontpellier.fr and sangsub@inha.ac.kr

¥ Co-first authors

Keywords

metal oxide nanowire, semiconductor metal oxide, gas sensing mechanism, humidity resistance, porous shell formation

Abstract

We report a novel route for enhancing the humidity resistance of SnO_2 nanowires (NWs; widely used metal oxide semiconductor gas sensors) based on their coating with a humidity-resistant nanomembrane. A conformal thin film was deposited by Molecular Layer Deposition (MLD) on the SnO_2 NWs using trimethylaluminum and ethylene glycol as precursors (100 MLD cycles), followed by oxidation in air at 400 °C. In conditions of increasing relative humidity, the SnO_2 NW gas sensor coated with a microporous, 10-nm thick nanomembrane layer of converted alucone obtained by MLD and calcination showed a remarkable gas response compared with the pristine SnO_2 NW gas sensor. This sensor was stable and displayed good recovery times in humid conditions (30 and 90% of relative humidity). This work shows the benefits and the practical application of MLD-prepared nanomaterials. This original strategy applied to NW-based gas sensors paves the way for other complex 3D designs and different applications that require gas or ion selectivity, such as photocatalysts and biosensors, in humid atmosphere.

Introduction

In recent years, the demand for gas detection and measurement devices has strongly increased, mostly for safety and environmental monitoring[1]. Semiconducting metal oxides (SMOs) are frequently used for the production of gas sensors because of their simple fabrication, good stability, stoichiometirc tunability, and excellent sensitivity towards many different gas molecules [1–4]. The gas sensor surface characteristics, e.g. composition, crystallinity, and microstructure (porosity, roughness), are directly related to its gas sensing performance, and therefore strongly influence the sensor features, particularly its selectivity, response and recovery times. Among the different metal oxide-based sensors, SnO_2 nanowires (NWs) are fast, stable, sensitive and reliable gas sensors that can be easily combined into a multi-component array [5]. However, SnO_2 and other metal oxide-based gas sensors present relatively low response and selectivity in realistic conditions of humid atmosphere, limiting their practical use. Hence, research efforts are still needed to tackle this key challenge. Among the different approaches, innovative nanomembrane materials could be used to improve the gas sensor performances in humid atmosphere conditions.

Recent studies have shown that aluminium alkoxide-based materials could be a potential candidate to improve the response of gas sensing in humid conditions [6–11]. In fact, Aluminium alkoxide, better known as alucone, is the most commonly synthesized material by Molecular Layer Deposition (MLD), using a well-developed process with trimethylaluminum (TMA) as precursor and ethylene glycol as co-reactant [12]. MLD is an Atomic Layer Deposition (ALD)-derived method based on sequential and self-limiting surface reactions [13]. ALD is a vapour phase deposition technique for the preparation of inorganic nanomaterials, such as oxides[14], nitrides[15,16] and metals[17,18], with sub-nanometric control of the thickness [19] and competitive mechanical response [20,21]. One of the main advantages of

these deposition methods is the excellent substrate uniformity and conformality over the surface even for the most complex 3D nanostructures [19,22,23].

The deposition of nanoscale films has become essential for many applications, especially in microelectronics[24,25] and catalysis,[26,27] but also membranes[28–30] and sensors[31]. MLD allows the preparation of conformal thin films (either hybrid organic–inorganic or purely organic films) using an organic compound instead of the classical ALD precursors [13]. Moreover, the addition of an etching or calcination post-treatment allows removing the organic component from the film, resulting in a porous inorganic matrix. MLD conformality control and the transformation of the prepared organic–inorganic films into porous (inorganic) ultrathin layers allow the synthesis of porous oxide nanomembranes. This microporous alumina layer could be valuable for enhancing the selectivity and stability of sensors and membrane devices [32,33]. The layer thickness can be modulated by varying the number of MLD cycles, and the pore dimensions can be tuned by controlling other experimental parameters, such as the organic reactant chemistry [32,34]. Jiang *et al.* prepared nanomembranes for gas separation by MLD (200 cycles) following by calcination of the organic template. These membranes display an He permeance of 5.3 $cm^3/bar \cdot cm^2 \cdot min$, and He/N_2 and He/SF_6 selectivities higher than 10^3 and 10^4, respectively [35]. By coating zeolite membranes (initial support) with microporous nanomembranes using MLD, Yu *et al.* prepared defect-free, microporous Al_2O_3/SAPO-34 zeolite composite membranes with very high H_2/N_2 selectivity compared with uncoated SAPO-34 membranes (1040 *versus* 8) [36].

Here, we describe a novel approach for improving the gas sensing performance of widely used SMO-based sensors in humid atmosphere. Specifically, the SnO_2 NW surface was coated with a microporous nanomembrane layer obtained by MLD of conformal alucone films using TMA and ethylene glycol as precursors, followed by oxidation in air at 400 °C. This approach for improving humidity resistance that relies on the protective effect of converted alucone

nanomembranes has never been described before. The optimized alucone-coated SnO_2 NW gas sensors exhibited good recovery time in humid atmosphere.

Experimental

Fabrication of the sensing devices:

To facilitate their potential integration into devices, sensors were produced using typical microelectronic fabrication routes. First, patterned interdigital electrodes (PIEs) were prepared on SiO_2-Si (100) substrates using a photolithographic technique. PIEs consisting of Au (3 nm)/Pt (200 nm)/Ti (50 nm) were sequentially sputter deposited onto the substrates. The Ti layer was used to improve the adhesion between the substrate and the Pt electrode layer. Using the vapour-liquid-solid growth technique, networked SnO_2 NWs were successively obtained on the previously deposited PIEs. For SnO_2 NW growth, Sn powder (99.9%) was put in a crucible that was introduced with the Si substrates supporting the PIEs into a quartz tube furnace at 900 °C for 5 min in the presence of nitrogen (300 standard cubic centimetre per minute, sccm) and oxygen (10 sccm).

Molecular layer deposition and calcination:

MLD was performed using a home-built ALD reactor and TMA (98% purity, CAS: 75-24-1; Strem Chemicals, Inc.) and ethylene glycol (99% purity, CAS: 107-21-1). The container with ethylene glycol was heated to 70 °C and the TMA bubbler was maintained at room temperature. The deposition chamber was set at 130 °C. Each MLD cycle consisted of 0.1s pulse of TMA, 10s exposure, and 30s purge, followed by a 2s pulse of ethylene glycol, 10s exposure and 60s

purge with Argon. After MLD, samples were directly placed in a furnace and calcined at 400 °C (ramp rate = 1 °C/min) for 1h.

Physicochemical characterization

Field emission Scanning Electron Microscopy (SEM, Hitachi S-4800) and Transmission Electron Microscopy (TEM, JEOL ARM 200F (200 kV)) coupled to Energy-dispersive X-ray spectroscopy (EDX) were used for NW morphology and composition analysis. Pristine SnO_2 NW and alucone-coated SnO_2 NW samples were immersed in ethanol and then laser scratched in a low-power sonication bath. Ethanol drops were collected, casted drop-by-drop on commercial Cu-grids and dried in a membrane pump (<10 bar) overnight. The sample chemical composition was further analysed by SEM (Zeiss EVO HD microscope) coupled to EDX (Oxford, X-Max N) and X-ray Photoelectron Spectroscopy (XPS, ESCALAB 250 Thermal Electron) with Al-Kα (1486.6 eV). Binding energies were calibrated with carbon (C 1s = 284.4 eV), and a surface of 500 μm^2 was analysed by XPS.

Gas sensing measurements:

The gas sensing performances of pristine and alucone-coated SnO_2 NW samples were compared by exposing them to different gases at various temperatures, in a horizontal gas-sensing system. The target gases were introduced in the gas-sensing system at specific concentrations obtained by mixing the dry air-balanced gas with dry synthetic air through accurate mass flow controllers. The total flow rate was set at 500 sccm. The sensor resistance was monitored using an electrical measurement system (Keithley 2400) interfaced with a computer. The sensing test was extensively described in our previous articles [9,23]. After

recording the resistance in air (R_a) and the resistance in the presence of the target gas (R_g), the sensor response (R) was calculated as $R = R_a/R_g$ (for reducing gases, such as CO, H_2, NH_3, C_6H_6, C_7H_8, ethanol) and $R = R_g/R_a$ (for oxidizing gases, such as NO_2). To study the effects of humidity, gas sensing measurements were performed in dry and in humid air (relative humidity (RH) of 0-90%, measured at 20 °C) at the sensor operating temperature of 300 °C.

Results and discussion

1. Sensor fabrication and characterization

SMO gas sensors are widely used and are typically integrated in miniaturized packages with other silicon-based elements. The main sensing device architecture, based on SnO_2 NWs grown on PIEs, is shown in the SEM images of Figure 1.

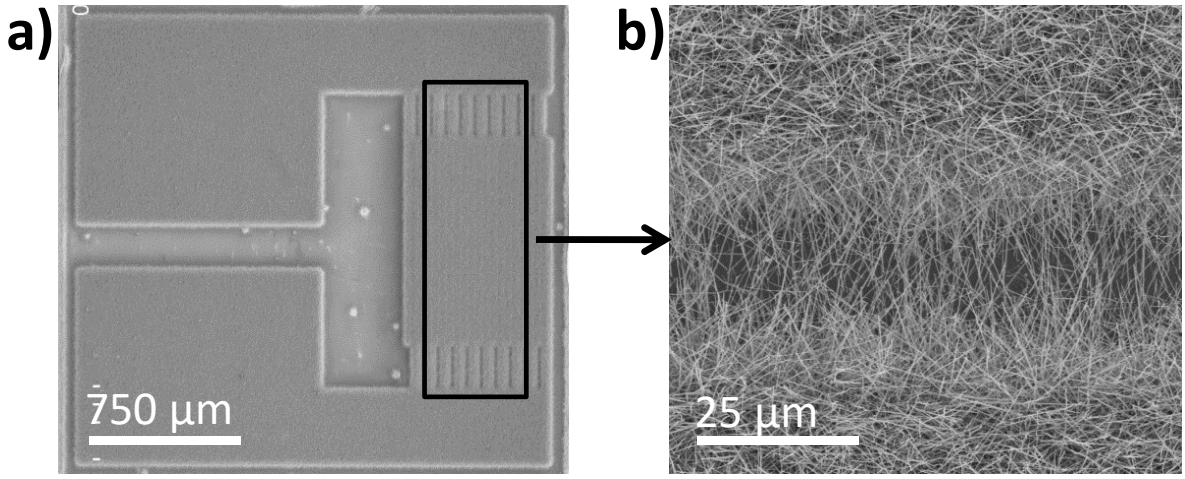

Figure 1. SEM images of the prepared SnO_2 NW sensor. (a) Top view, and (b) SEM image of the synthesized nanowires.

The highly networked SnO_2 NWs extended from one side to the other of the electrodes (Figure 1b). SnO_2 NW growth on the surface of the PIE pads was obtained using the vapour-liquid-solid method, a catalyst route. Metallic Sn powder (99.9%) was heated to 900 °C, and the flow profiles of the source vapours were optimized, because they can affect the overall formation of NWs. Indeed, the careful tuning of vapour flows is crucial for solid sources of SnO_2 vapours, because highly variable NW density and length can be obtained [37].

Next, the growth of poly (aluminium ethylene glycol) polymer (better known as aluminium alkoxide, or simply alucone) films, was performed by MLD. Various films were prepared, by sequential exposures of TMA and ethylene glycol. Figure 2 is a schematic illustration of the MLD process used in this work.

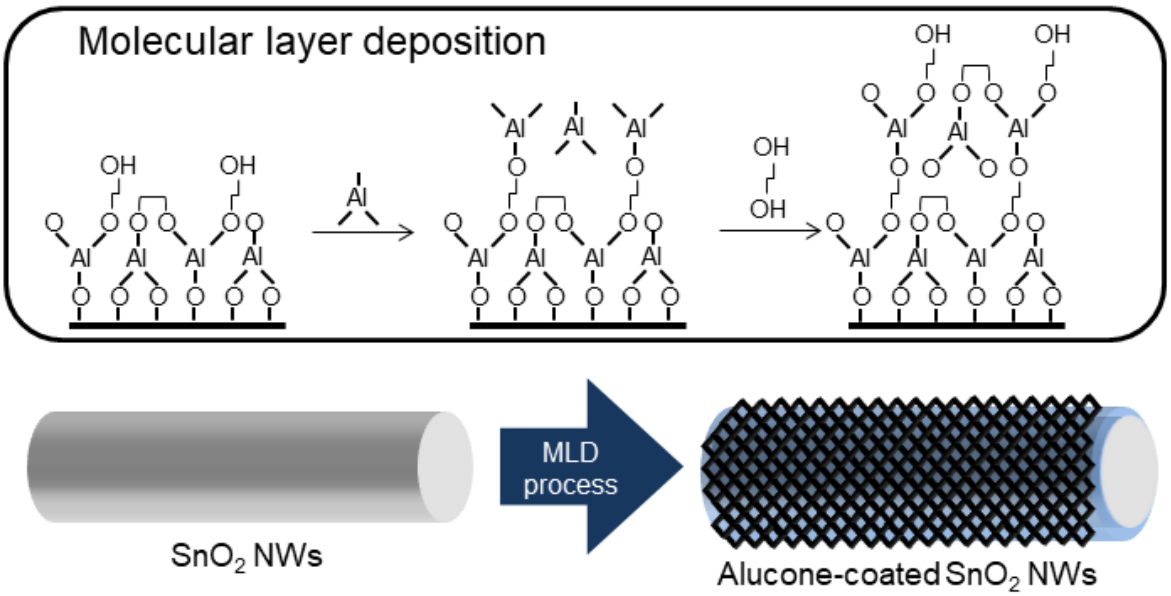

Figure 2. Schematic illustration of the MLD process for the preparation of the alucone-coated SnO_2 NWs used in this work.

Different numbers of MLD cycles (10, 50, and 100) were used to coat with alucone the SnO_2 NW surface at 130 °C, resulting in conformal hybrid alucone layers of different thickness. MLD was directly followed by calcination to convert the hybrid nanolayers to the desired alumina nanomembranes because the air and water present in the atmosphere quickly and permanently degrade the MLD-deposited alucone material[12,33]. Calcination was carried out at 400 °C to ensure the successful conversion of CH_2-CH_2 bonding to CO_2 and H_2O. It has been demonstrated that after oxidation in air at 400 °C of alucone films made of TMA and ethylene glycol, micropores with a diameter of around 0.6 nm are created [33,34,38]. This is due to the removal of the monolayer of ($–CH_2CH_2–$) groups, presenting this dimension [12,13]. However, it is important to note that although the length of the organic chains of the organic co-reactant has a major influence on the pore dimensions, [39] other parameters involved in etching/calcination also can have an effect. For example, the film porosity has been linked to the applied temperature ramp rate [34]. Therefore, many different porous oxide films with controlled thickness can be synthesized by thermal treatment of MLD-prepared thin films. These oxide nanostructures can have high surface areas (more than 1000 m^2/g) [32]. After sample preparation, EDX mapping was performed to verify the sensor elemental composition and the presence of the alumina nanomembrane.

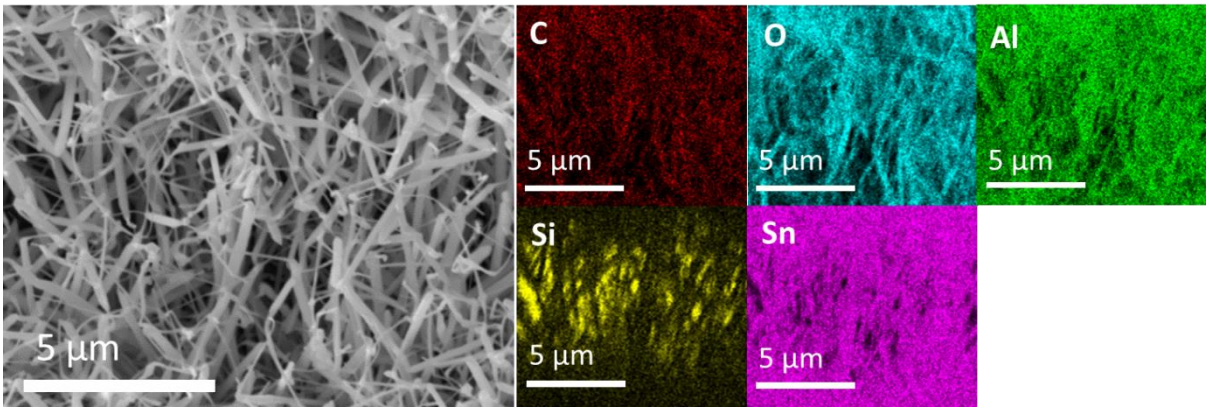

Figure 3. SEM image of the sensor (left panel) and EDX mapping indicating the distribution of C, O, Al, Si and Sn (right panels).

The NWs presented a diameter between 50 and 300 nm (mean value: ~175 nm), and their length typically reached several microns (Figure 3 and Figure S1). The forest of nanowires visible in the SEM image allowed their interconnection, which is beneficial for the good conduction of electrical signals. Moreover, the EDX mapping results (Figure 3) clearly highlighted the presence of C, O, Al, Si and Sn elements.

In addition, the composition and the oxidation level of alumina membrane coated SnO_2 NWs were analysed by XPS. All the expected elements (Sn, Al, O) were found as well as carbon, which can be explained by the surface contamination between NWs. Figure 4 shows the XPS scans of Sn 3d and Al 2p in alumina membrane coated SnO_2 NWs.

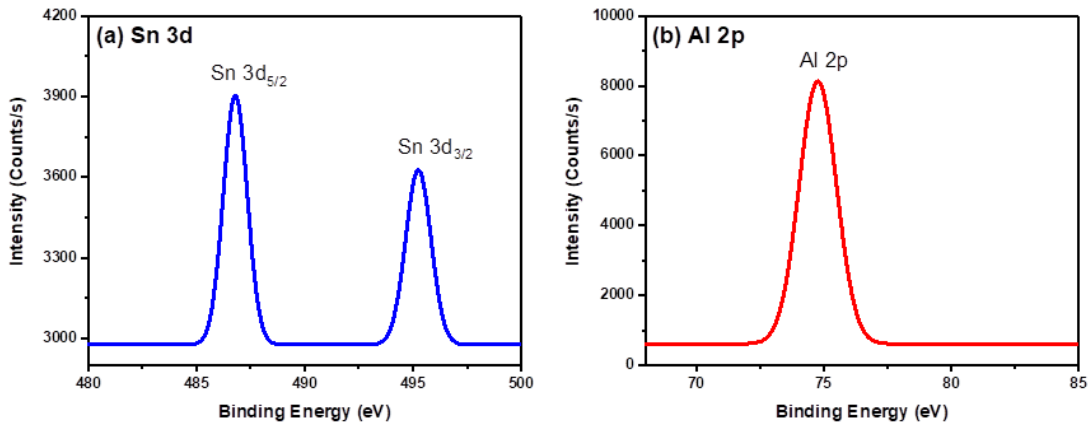

Figure 4. High-resolution XPS spectra of the (a) Sn 3d and (b) Al 2p levels of the alumina membrane coated (100 MLD cycles of alucone) SnO_2 NW sensor.

Finally, the morphology of SnO_2 NWs coated with alumina nanomembranes (10, 50 and 100 cycles of alucone) was studied by high resolution TEM (Figure 5a-c). This revealed the presence of amorphous alumina nanomembranes conformably covering the SnO_2 NWs. The

nanomembrane thicknesses was approximately 2 nm, 5 nm and 10 nm for the samples prepared using 10, 50 cycles and 100 cycles of alucone, respectively. Importantly, although the diameter distribution of the SnO_2 NWs was large, the film conformal growth remained homogeneous over the whole sample.

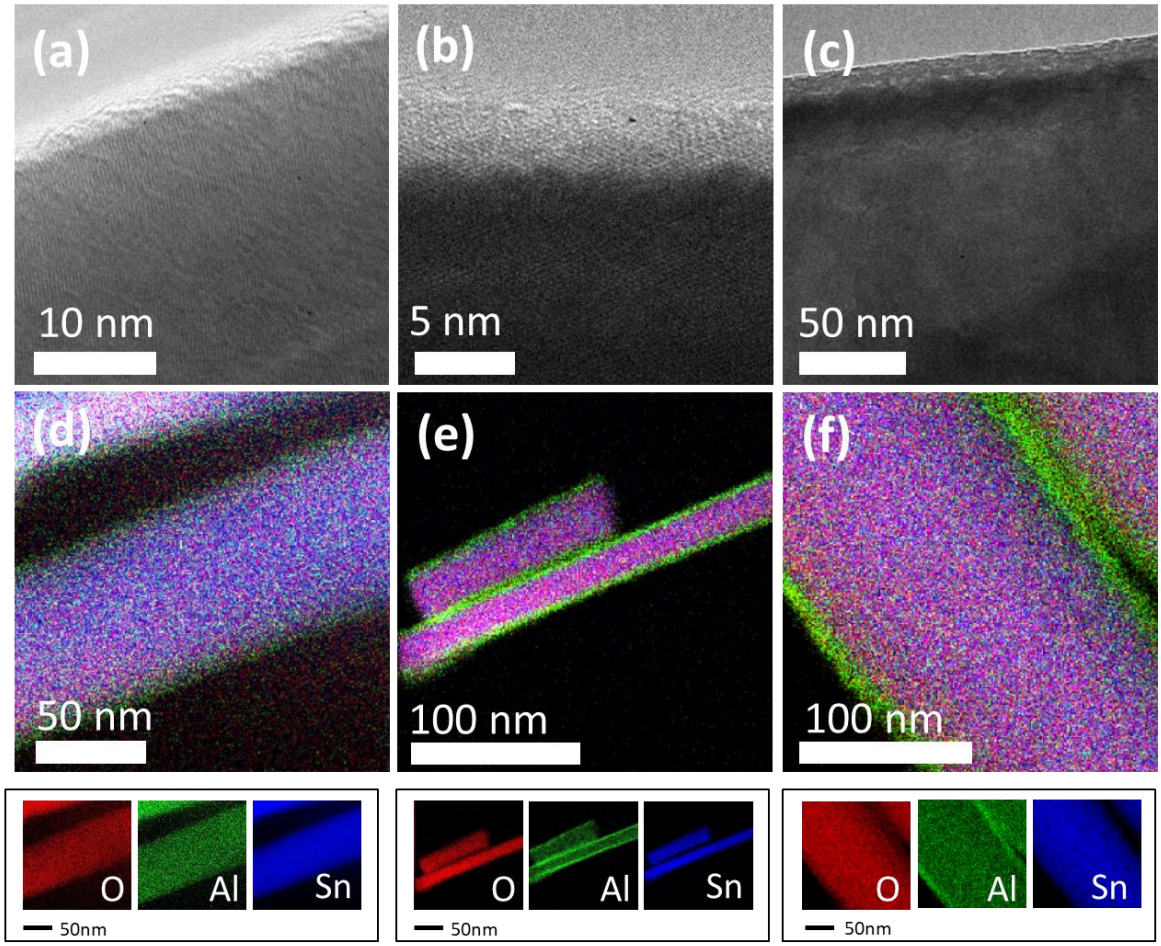

Figure 5. TEM images of NWs coated with alumina nanomembranes prepared using (a) 10 cycles, (b) 50 cycles, and (c) 100 cycles of MLD. The corresponding EDX maps are in (d), (e) and (f).

The alucone theoretical growth rate (~0.50 nm per cycle)[40] should result in much thicker layers; however, the layers obtained in this work were much thinner. This is not surprising, because the oxidation of MLD-prepared layers leads to a structural collapse through the

formation of the alumina nanomembrane. Moreover, the water present in the atmosphere also contributes to degrade MLD layers and to quickly decrease their thicknesses. In addition, our results are in good agreement with what previously reported. For example, Weimer's group deposited alucone by MLD on particles and showed that if a porous film persisted on the particle surface after oxidation, the film thickness was greatly reduced from 25 nm to 8 nm [33].

2. Gas sensing results and possible mechanism(s) of the enhanced humidity resistance

The gas sensing performance of the prepared devices was then tested. The alumina nanomembrane coated SnO_2 NWs sensor is schematically described in Figure 6a. It shows the electrical conduction channel of the networked SnO_2 NW structure grown on neighbouring PIE pads. The gas-sensing properties of the SnO_2 NWs gas sensor coated with alumina nanomembrane (100 cycles of alucone, 10 nm thickness) was tested in the presence of three concentrations (10, 50 and 100 ppm) of NO_2 gas in dry air at temperatures ranging from 250 to 400 °C. The transient normalized resistance curves of the sensor in the presence of various concentrations of NO_2 gas clearly demonstrated the n-type sensing behaviour of the sensor (Figure 6b for 100 ppm). This means that the introduction of an oxidizing gas, like NO_2, results in an increase of the sensor resistance that returns to baseline values upon interruption of the gas delivery, in good agreement with the well-known modulation behaviour in the conduction channel of NWs during the interaction of gas molecules and pre-adsorbed oxygen species on the NW surface. Analysis of the sensor response to NO_2 in function of the operating temperature (Figure 6c) indicated that the maximum sensing responses was obtained at 300 °C for all NO_2 concentrations in dry air. This behaviour of the optimal sensitivity at a certain sensing temperature is often observed in chemiresistive-type gas sensors. This is because the interaction between adsorption and desorption of gas molecules onto the sensor material is optimized at that temperature. The SnO_2 NWs gas sensor coated with alumina nanomembrane exhibits its

highest response at 300 °C. In case the temperature is less than 300 °C, the NO_2 gas molecules do not have sufficient energies for adsorption onto the sensing material. In sharp contrast, if the temperature is greater than 300 °C, the desorption of NO_2 gas molecules becomes more dominant. The adsorption rate and desorption rate are likely to be balanced at 300 °C, resulting in the highest sensor response. Therefore, all the sensing responses were measured at this temperature. It should be mentioned that the operating temperatures vary between oxidizing and reducing gases. Typically, the highest gas-sensing response is observed at higher temperatures for reducing gases. Therefore, for a more detailed and precise analysis of the gas sensing performance, the operating temperature should be optimized for oxidizing and reducing gases before testing, which could be a new research topic.

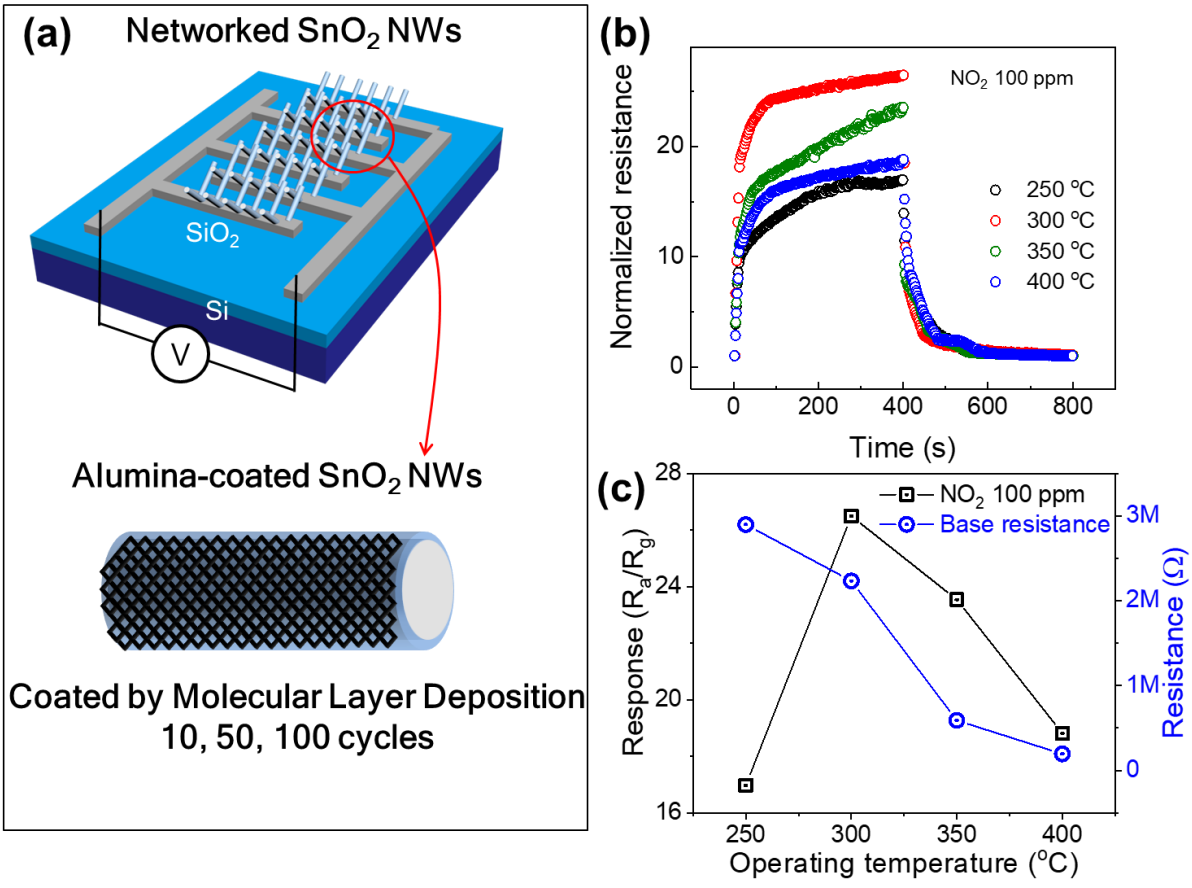

Figure 6. (a) Schematic illustration of the alumina coated SnO_2 NW gas sensor; (b) Normalized resistance curves of the sensor fabricated from alumina membrane coated SnO_2 NWs (100 cycles of alucone, 10 nm thickness) for NO_2 at the indicated temperatures; (c) Sensor response in function of the operating temperature.

Next, the gas-sensing behaviour of the alumina coated SnO_2 NW sensors was investigated in function of the alumina shell layer thickness (2 nm, 5 nm and 10 nm) and for different gases (NO_2, CO, H_2, NH_3, C_6H_6, C_7H_8 and ethanol) (Figure 7). The resistance curves clearly varied in function of the alumina thickness. Similarly, the sensing response (Figure 8) decreased as the alumina layer thickness increased. It is likely that in sensors coated with thicker alumina layers, the direct interaction of gas molecules with the SnO_2 NW surface of the active sensing material becomes more hampered in comparison with the case of thinner alumina layers, thus suppressing the sensor response as the thickness of the alumina layer increases. Overall, the response to NO_2 was higher than all other tested gases with all sensors (Figure 8).

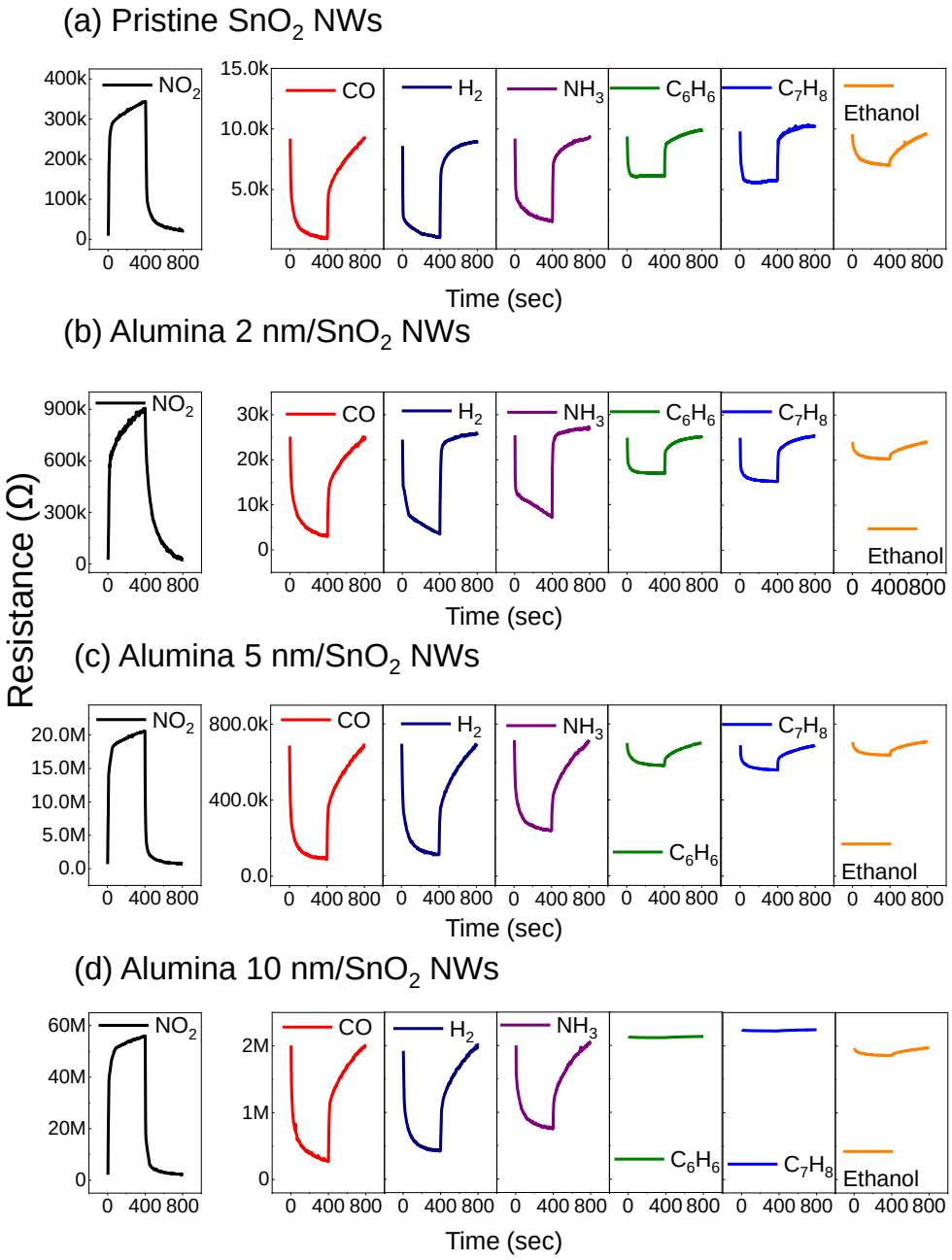

Figure 7. Transient resistance curves of the SnO_2 NW sensors coated with an alumina layer of different thickness for various gases measured at the optimized temperature of 300 °C; (a) pristine SnO_2 NWs, (b) SnO_2 NWs with 2nm-thick, (c) SnO_2 NWs with 5nm-thick, and (d) SnO_2 NWs with 10nm-thick alumina layer.

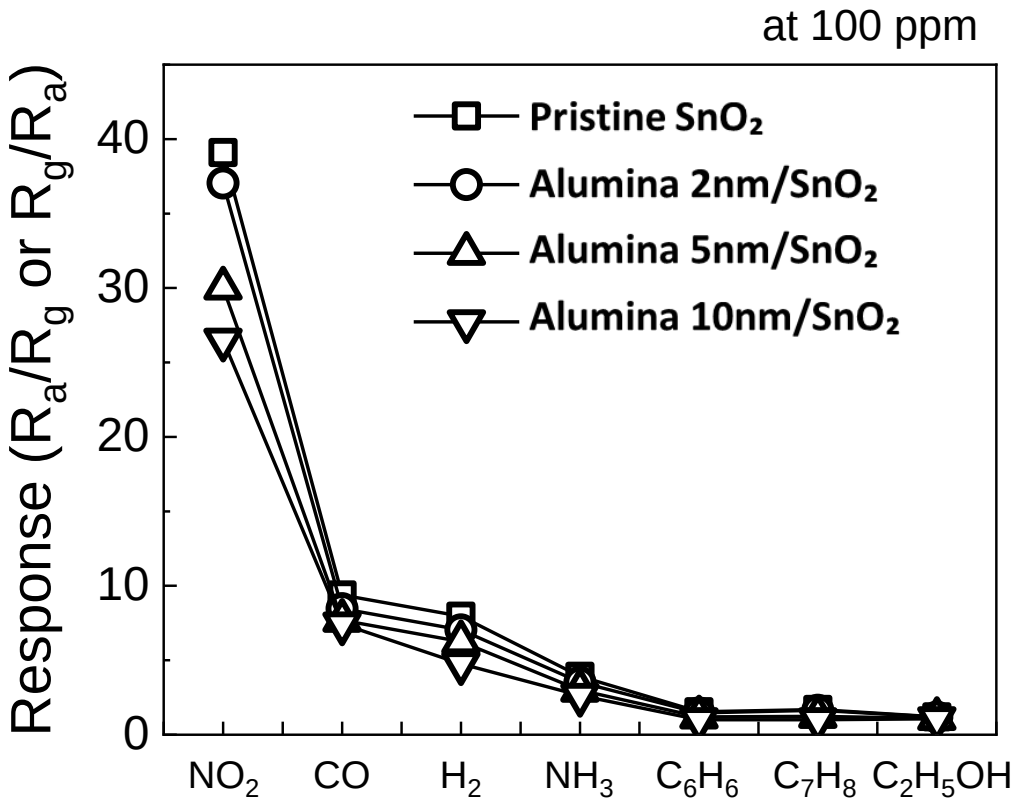

Figure 8. Alumina nanomembrane-coated SnO_2 NW sensor responses to various gases. Pristine SnO_2 NW sensors and coated with an alumina shell layer of the indicated thickness were used.

In real applications, sensing devices always interact with water molecules in air, particularly in humid atmospheres. For this reason and to demonstrate the practical use of the sensors, the transient resistance curves and the response of pristine and alumina-coated SnO_2 NW gas sensors (different alumina shell layer thicknesses) to 100 ppm of NO_2 gas were determined at different relative humidity values (RH 0 to 90%) and at the optimum operating temperature (300 °C), (Figures 9 and 10).

(a) Pristine SnO_2 NWs

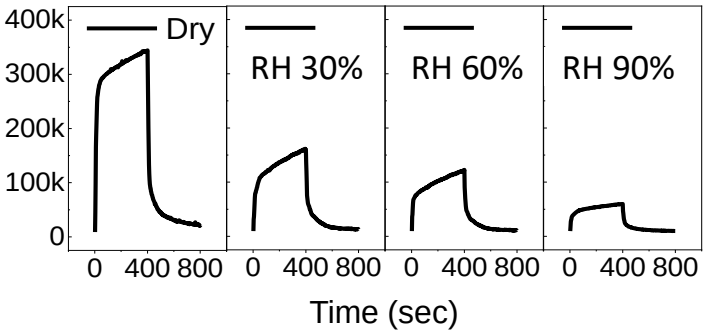

Time (sec)

(b) Alumina 2 nm/SnO_2 NWs

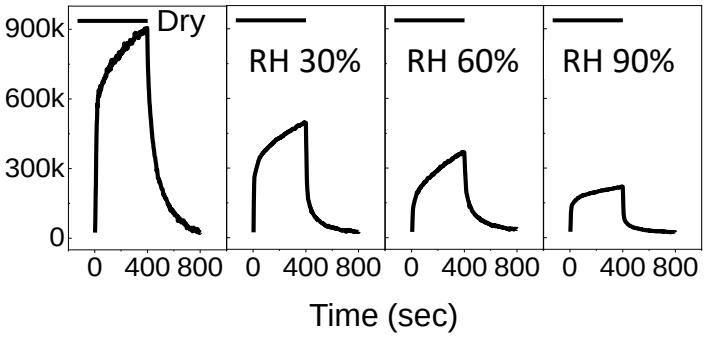

Resistance (Ω)

Time (sec)

(c) Alumina 5 nm/SnO_2 NWs

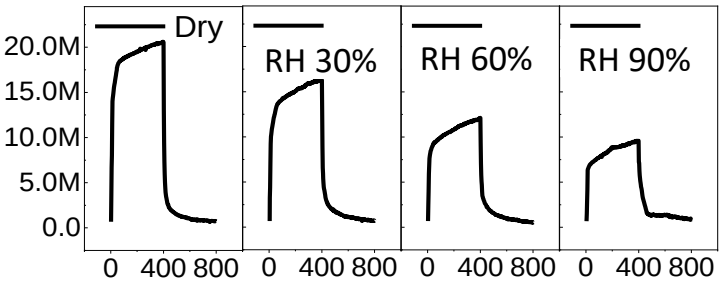

Time (sec)

(d) Alumina 10 nm/SnO_2 NWs

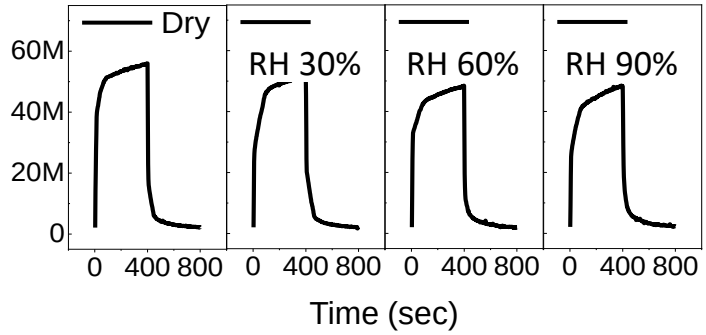

Time (sec)

Figure 9. Transient resistance curves of SnO_2 NW sensors for NO_2 (100 ppm) at 300 °C and the indicated relative humidity. (a) Pristine SnO_2 NWs, (b) SnO_2 NWs with 2nm-thick, (c) SnO_2 NWs with 5nm-thick, and (d) SnO_2 NWs with 10nm-thick alumina layer.

These data indicated that with the RH% increase, the gas sensor response decreased, as previously reported [41]. This effect was observed when using pristine SnO_2 NWs and also, to a lower extent, with SnO_2 NWs coated with 2nm-thick and 5nm-thick alumina layer (Figure 9a-c), but was negligible with SnO_2 NWs coated with a 10nm-thick alumina layer (Figure 9d). The transient resistance curves and the responses of pristine and alumina-coated SnO_2 NW sensors for various gases (100 ppm) in function of the relative humidity are shown in Figures S2-S5 and Figure S6, respectively.

For networked NW sensors, resistance changes can be explained by (1) modulation in contact resistance between NWs, and (2) radial modulation of the conduction layer in NWs [42,43]. In the case of smaller diameter than the Debye length, the whole region of NWs becomes depleted in carrier concentration, resulting in a high initial resistance, and the resistance change is likely to originate largely from the modulation in contact resistance. Conversely, if the NW diameter is larger than the Debye length, the NW region will be only partially depleted, and the modulation of the conduction layer in NWs is the dominant source. By taking into account the Debye lengths of SnO_2 NWs (~18 nm) [44,45] in similar sensing measurement conditions, it is reasonable to conclude that the SnO_2 NWs used in this study were partially depleted. This indicates that the main source of resistance change in the alumina membrane coated SnO_2 NWs is the radial modulation of the conduction layer in NWs. The underlying sensing mechanism was extensively discussed in our earlier reports[46,47]. Therefore, it is reasonable to think that the resistance change is caused by the modulation in

width of the depletion layer along the length direction of single-crystalline SnO_2 nanowires. However, the modulation in contact resistance between NWs also should be considered as a significant source of resistance change observed in alumina coated NWs. The contacts between NWs can play a similar role as grain boundaries in bulk or film-type sensing materials. Oxygen and target gas molecules can be adsorbed into contact areas between NWs, eventually resulting in a considerable resistance modulation during the adsorption and desorption of gas molecules. Importantly, as NWs form a simple mechanical contact with each other and mutual displacements of NWs may occur during alucone deposition and annealing, the alucone layer can be deposited between SnO_2 NW contacts. Accordingly, NW contacts can be a more important source of resistance modulation.

In addition, we investigate here the deposition of alucone by MLD on SnO_2 NWs. TMA first reacts with hydroxyl groups on SnOH to deposit Al-CH_3 surface species. Ethylene glycol then reacts with Al-CH_3 species to deposit –CH_2CH_2OH surface species. Nevertheless, many parameters could affect the growth rate and the conformal layer deposition, such as the density of available reactive sites on the surface and the steric effects of the optimum saturation occupancy of those sites. Steric hindrance of the ligands and the number of reactive surface sites are among the major factors that could affect the growth per cycle [48]. In our experimental conditions, part of the surface of SnOH ligands might have been not accessible to the reactant because of steric hindrance, leaving available sites for gas detection. Moreover, the alucone layer deposited by MLD was calcined. The obtained porous alumina membrane had a pore size (~0.6 nm) that was large enough for all the tested gas molecules, except NH_3, to penetrate toward the n-SnO_2 surface. Therefore, it could be hypothesized that the SnO_2 NWs are only partially covered rather than completely covered by the alumina layer. Thus, the improvement in gas sensing performance is due to the depletion region created on the interface of the heterojunction of the two semiconductors when the electron and hole carriers inter-diffuse [49].

The alumina membrane provide additional accessible surface area and grain boundaries that contribute to the enhanced sensing response via the effective and quick diffusion of gas vapour into the sensing membranes [50].

After heat treatment, alucone deposited on n-type SnO_2 NWs is transformed into alumina membrane that behaves like a typical dielectric material with a very low concentration of charge carriers. Therefore, the band diagram of the insulating Al_2O_3-n-type SnO_2 heterostructure must be constructed. Accordingly, NWs consisting of the insulation shell and semiconducting core should show higher resistance compared with pristine n-type SnO_2 NWs without the insulation shell. For this reason, the deposition of alumina membrane resulted in the large increase in resistance of the sensor observed in this study. Of note, the large increase in resistance is disadvantageous for the actual sensor applications.

As the pores of the alumina membrane layer were large enough for the tested gas molecules to penetrate toward the surface of n-SnO_2 (Figure 10b), the radial modulation of the conduction layer in core SnO_2 NWs can be considered the dominant sensing mechanism, which is basically the same as for pristine n-SnO_2 NWs, although the conduction layer is contracted. A similar sensing behaviour was observed in metal-organic framework-based membrane encapsulated ZnO NWs [51,52].

The kinetic diameters of the tested gas molecules (NO_2, CO, H_2, NH_3, C_6H_6, C_7H_8, and ethanol) were 0.34, 0.376, 0.289, 0.260, 0.585, 0.585, and 0.45 nm, respectively [53,54]. On the other hand, the kinetic diameter of water molecules is 0.28 nm,[54] which is smaller than what obtained with all tested gas molecules except NH_3. As the pore diameter of the alumina membrane layer was estimated to be ~0.6 nm, it is reasonable to conclude that both the tested gases and water molecules can penetrate through the porous alucone layer (Figure 10b). Therefore, another reason to explain the improvement of humidity resistance by the formation

of the alumina layer should be considered. It is known that Al_2O_3 or Al_2O_3/alucone layers deposited by ALD strongly decrease water vapour transmission [6,8,33,55]. Al_2O_3 layers can drastically improve the water vapour diffusion barrier property possibly by increasing the water vapour diffusion path in the film and by decreasing the diffusion speed by trapping water vapour chemically. The hydrophobic nature of alumina/SnO_2 prepared sensor plays vital role to avoid the water vapor adsorption on oxide surface during gas exposure, which leads to fast response/recovery and baseline stability of the sensor.

It was shown that the alucone coating is hydrophilic, but its conversion into a microporous structure allows its conversion to a hydrophobic surface [56]. Interestingly, *Mavric et al.* have recently found that the structure of alumina could change with the synthesis conditions. In fact, they reported that hydrophobicity of alumina is directly affected by the crystallinity of the layer. They found that polycrystalline structure were hydrophilic while amorphous form was hydrophobic. This funding is in good agreement with our research, whereas alumina membrane is amorphous [57]. As hydrophobic membranes "hate" or repel water, they are typically used in gas filtration processes [58]. For instance, *Hu et al.* found that the sensing response toward HCl remains unchanged when varying the relative humidity from 10 to 90%. They showed that their sensor surface is hydrophobic and this explains the sensor stability in different conditions of humidity [59]. Moreover, *Liu et al.* confirmed that higher hydrophobic materials have better waterproof effect. This means that due to the membrane hydrophobicity, water vapours cannot penetrate the membrane. However, the tested gases need to permeate the membrane to get in touch with SnO_2. As all the tested gases had a diameter smaller than that of alumina micropores (except NH_3), they could penetrate the membrane and get in touch with SnO_2, whereas hydrophobic nanoporous alumina will inhibit water vapour penetration by repelling it on the surface to limit the influence of water vapour [60] (Figure 10b).

Comparison of the response and recovery times of the sensors to 100 ppm NO_2 at 300 ℃ and RH 90% (Figure S7) showed that the 10 nm alumina coated SnO_2 NWs sensor had the shortest response and recovery time in humid conditions. In general, the presence of an additional layer that prevents the penetration of gas molecules to the sensitive layer should be accompanied by an increase in the response and recovery times. However, this was not observed in the present experiments, suggesting that there is another sensing mechanism that controls the gas-sensing effect. In humid environments, water molecules are competitively adsorbed on the sensor material surface and this hampers the reaction of target gas molecules with the sensor material. Conversely, once a porous Al_2O_3 layer is formed on the sensor material, water molecules are preferentially blocked by the layer compared with other target gases. This facilitates the reaction of gas molecules with the sensor material. This explain the shorter response and recovery times of 10 nm thick alumina-coated NWs. Based on our results, it is possible to design other nanomembrane-coated SMO NW gas sensors that could be employed to improve their gas sensing activity in humid conditions for practical applications.

Humidity-resistant gas sensors based on SnO_2 materials have been extensively studied. For example, mesoporous SnO_2 hierarchical architectures show H_2S detection at low concentrations (ppb) in highly humid atmosphere (RH = 85%) [61]. Thin-walled SnO_2 nanotubes show good detection of H_2S in very humid atmosphere by the formation of clustered pores [62]. A negligible humidity dependence of the sensor signal was observed using CuO-loaded SnO_2 hollow spheres at RH = 80% [63]. In our study, a molecular nanomembrane was used to increase humidity resistance of SnO_2 NW gas sensing properties, a novel and completely different approach compared with the previous reports [61–63].

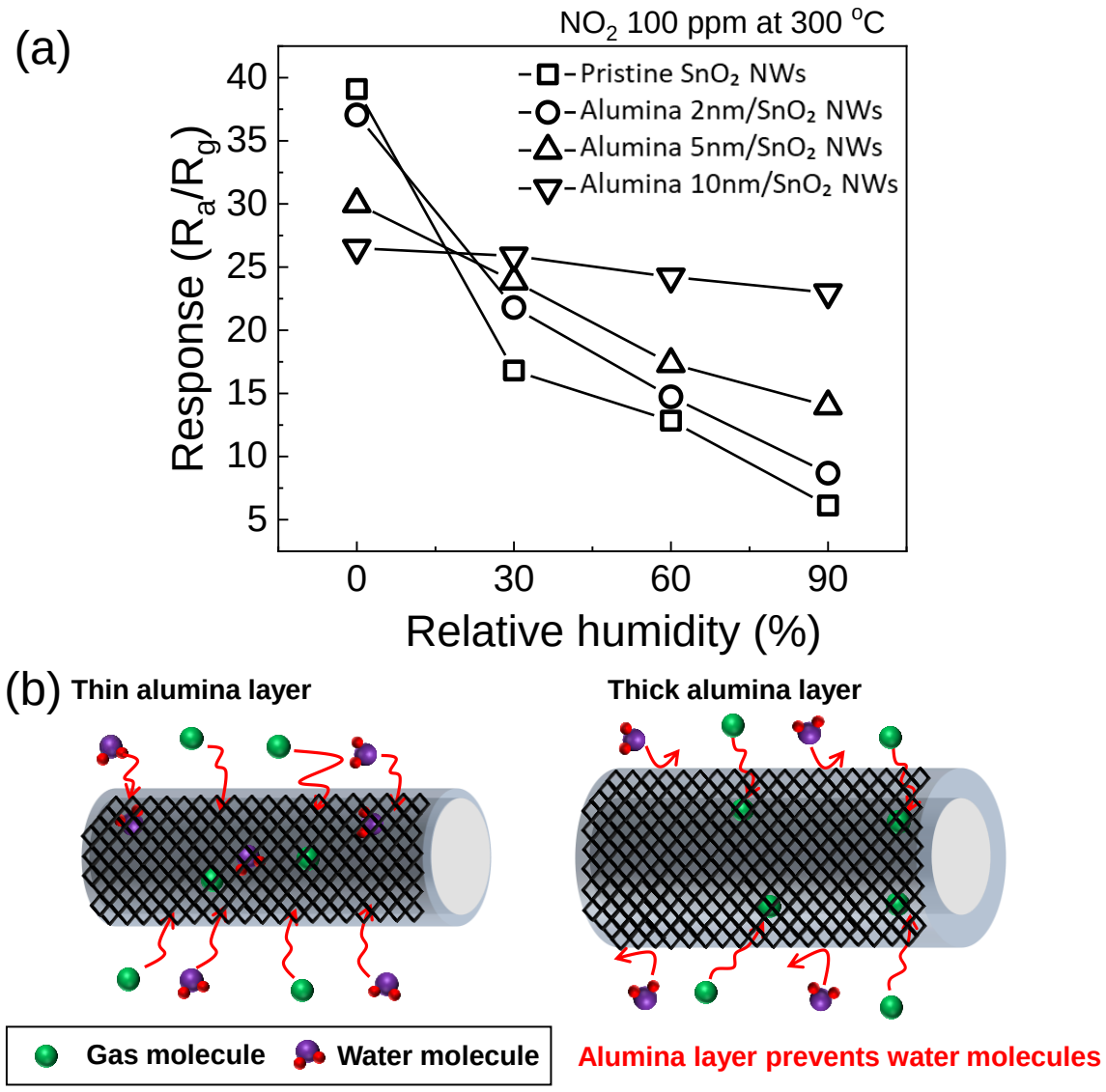

Figure 10. (a) The responses of gas sensors to NO_2 (100 ppm) in function of the relative humidity. (b) Schematic illustration showing the humidity resistance changes in function of the thickness of the alumina nanomembrane.

Conclusions

In this work, we presented a promising strategy for improving the gas sensing properties of metal oxide sensors in humid atmospheres. This novel approach is based on the encapsulation of SnO_2 NWs with a humidity-resistive nanomembrane obtained by calcinating MLD-prepared

alucone films. The control of channel size in alumina membrane is useful for preventing the crossing by water molecules, which leads to highly efficient and industrially viable gas sensing devices. Our results showed that the response to NO_2 gas of 10 nm alumina-coated SnO_2 NWs is comparable in dry air conditions and in various conditions of relative humidity (RH 30 to 90%). The thickness of the alumina membrane layer should be minimized to secure the best sensing performance under humidity conditions. The present results open the way for the fabrication of humidity-resistive gas sensors that could be used in the production, transportation or storage of this upcoming energy source.

Acknowledgments:

We would like to thanks the French national research agency (ANR, program MeNiNA-ANR-17-CE09-0049) and the Lebanese University for funding this project. Support by the COST Action MP1402 "HERALD", a European cooperation program, is acknowledged. I.I. acknowledges the partial financial support from the NCN of Poland by the SONATA 11 project UMO-2016/21/D/ST3/00962. This work was supported by the National Research Foundation of Korea (NRF) grant funded by the Korea government (MSIT) (2021R1A2C1009790).

References:

1. J. Zhang, X. Liu, G. Neri, N. Pinna, *Advanced Materials*, 28 (2016) 795–831.
2. H.-J. Kim, J.-H. Lee, *Sensors and Actuators B: Chemical*, 192 (2014) 607–627.
3. Y. Hong, C.-H. Kim, J. Shin, K.Y. Kim, J.S. Kim, C.S. Hwang, J.-H. Lee, *Sensors and Actuators B: Chemical*, 232 (2016) 653–659.
4. S. Ramanavicius, A. Ramanavicius, *Sensors*, 20 (2020).
5. Z. Cai, S. Park, *Sensors and Actuators B: Chemical*, 322 (2020) 128651.
6. M. Park, S. Oh, H. Kim, D. Jung, D. Choi, J.-S. Park, *Thin Solid Films*, 546 (2013) 153–156.

7. F. Nehm, H. Klumbies, C. Richter, A. Singh, U. Schroeder, T. Mikolajick, T. Mönch, C. Hoßbach, M. Albert, J.W. Bartha, K. Leo, L. Müller-Meskamp, *ACS Appl. Mater. Interfaces*, 7 (2015) 22121–22127.
8. D. Choi, M. Yoo, H.M. Lee, J. Park, H.Y. Kim, J.-S. Park, *ACS Appl. Mater. Interfaces*, 8 (2016) 12263–12271.
9. T. Nam, Y.J. Park, H. Lee, I.-K. Oh, J.-H. Ahn, S.M. Cho, H. Kim, H.-B.-R. Lee, *Carbon*, 116 (2017) 553–561.
10. S. Lee, G. Baek, J.-H. Lee, D.-W. Choi, B. Shong, J.-S. Park, *Applied Surface Science*, 458 (2018) 864–871.
11. V.V. Kondalkar, L.T. Duy, H. Seo, K. Lee, *ACS Appl. Mater. Interfaces*, 11 (2019) 25891–25900.
12. D. Choudhury, G. Rajaraman, S.K. Sarkar, *Journal of Vacuum Science & Technology A*, 36 (2018) 01A108.
13. P. Sundberg, M. Karppinen, *Beilstein Journal of Nanotechnology*, 5 (2014) 1104–1136.
14. J. Hämäläinen, M. Ritala, M. Leskelä, *Chem. Mater.*, 26 (2014) 786–801.
15. M. Weber, B. Koonkaew, S. Balme, I. Utke, F. Picaud, I. Iatsunskyi, E. Coy, P. Miele, M. Bechelany, *ACS Appl. Mater. Interfaces*, 9 (2017) 16669–16678.
16. M. Weber, E. Coy, I. Iatsunskyi, L. Yate, P. Miele, M. Bechelany, *CrystEngComm*, 19 (2017) 6089–6094.
17. M.J. Weber, A.J.M. Mackus, M.A. Verheijen, V. Longo, A.A. Bol, W.M.M. Kessels, *J. Phys. Chem. C*, 118 (2014) 8702–8711.
18. E. Coy, K. Siuzdak, M. Pavlenko, K. Załęski, O. Graniel, M. Ziółek, S. Balme, P. Miele, M. Weber, M. Bechelany, I. Iatsunskyi, *Chemical Engineering Journal*, 392 (2020) 123702.
19. S.M. George, *Chem. Rev.*, 110 (2010) 111–131.
20. M. Pavlenko, E. Coy, M. Jancelewicz, K. Załęski, V. Smyntyna, S. Jurga, I. Iatsunskyi, *RSC Advances*, 6 (2016) 97070–97076.
21. E. Coy, L. Yate, Z. Kabacińska, M. Jancelewicz, S. Jurga, I. Iatsunskyi, *Materials & Design*, 111 (2016) 584–591.
22. H. Van Bui, F. Grillo, J. Van Ommen, *Chemical Communications*, 53 (2017) 45–71.
23. M. Weber, J.-Y. Kim, J.-H. Lee, J.-H. Kim, I. Iatsunskyi, E. Coy, P. Miele, M. Bechelany, S.S. Kim, *J. Mater. Chem. A*, 7 (2019) 8107–8116.
24. I.J. Raaijmakers, *ECS Transactions*, 41 (2019) 3–17.
25. G.N. Parsons, S.M. George, M. Knez, *MRS Bulletin*, 36 (2011) 865–871.
26. M. Weber, P. Collot, H. El Gaddari, S. Tingry, M. Bechelany, Y. Holade, *ChemElectroChem*, 5 (2018) 743–747.
27. A.J.M. Mackus, M.J. Weber, N.F.W. Thissen, D. Garcia-Alonso, R.H.J. Vervuurt, S. Assali, A.A. Bol, M.A. Verheijen, W.M.M. Kessels, *Nanotechnology*, 27 (2015) 034001.
28. M. Weber, A. Julbe, A. Ayral, P. Miele, M. Bechelany, *Chem. Mater.*, 30 (2018) 7368–7390.
29. M. Weber, A. Julbe, S.S. Kim, M. Bechelany, *Journal of Applied Physics*, 126 (2019) 041101.
30. M. Weber, M. Drobek, B. Rebière, C. Charmette, J. Cartier, A. Julbe, M. Bechelany, *Journal of Membrane Science*, 596 (2020) 117701.
31. O. Graniel, M. Weber, S. Balme, P. Miele, M. Bechelany, *Biosensors and Bioelectronics*, 122 (2018) 147–159.
32. X. Liang, A.W. Weimer, *Current Opinion in Solid State and Materials Science*, 19 (2015) 115–125.
33. X. Liang, M. Yu, J. Li, Y.-B. Jiang, A.W. Weimer, *Chemical Communications* (2009) 7140–7142.
34. K. Van de Kerckhove, M.K. Barr, L. Santinacci, P.M. Vereecken, J. Dendooven, C. Detavernier, *Dalton Transactions*, 47 (2018) 5860–5870.
35. Y.-B. Jiang, G. Xomeritakis, Z. Chen, D. Dunphy, D.J. Kissel, J.L. Cecchi, C.J. Brinker, *J. Am. Chem. Soc.*, 129 (2007) 15446–15447.
36. M. Yu, H.H. Funke, R.D. Noble, J.L. Falconer, *J. Am. Chem. Soc.*, 133 (2011) 1748–1750.
37. M.H. Asif, A. Razaq, N. Akbar, B. Danielsson, I. Sultana, *Materials Research Express*, 6 (2019) 095028.
38. Z. Shang, (2017).

39. X. Liang, B.W. Evanko, A. Izar, D.M. King, Y.-B. Jiang, A.W. Weimer, *Microporous and Mesoporous Materials*, 168 (2013) 178–182.
40. X. Liang, D.M. King, P. Li, S.M. George, A.W. Weimer, *AIChE Journal*, 55 (2009) 1030–1039.
41. J.-H. Lee, J.-Y. Kim, J.-H. Kim, S.S. Kim, *Sensors*, 19 (2019).
42. J.Y. Park, S.-W. Choi, S.S. Kim, *J. Phys. Chem. C*, 115 (2011) 12774–12781.
43. J.-S. Lee, A. Katoch, J.-H. Kim, S.S. Kim, *Journal of Nanoscience and Nanotechnology*, 16 (2016) 11580–11585.
44. S.-W. Choi, A. Katoch, J.-H. Kim, S.S. Kim, *ACS Appl. Mater. Interfaces*, 6 (2014) 17723–17729.
45. S.-W. Choi, A. Katoch, J.-H. Kim, S.S. Kim, *J. Mater. Chem. C*, 3 (2015) 1521–1527.
46. A. Katoch, S.-W. Choi, G.-J. Sun, H.W. Kim, S.S. Kim, *Nanotechnology*, 25 (2014) 175501.
47. S.-W. Choi, A. Katoch, G.-J. Sun, J.-H. Kim, S.-H. Kim, S.S. Kim, *ACS Appl. Mater. Interfaces*, 6 (2014) 8281–8287.
48. R.L. Puurunen, *Journal of Applied Physics*, 97 (2005) 121301.
49. W.C. Ko, K.M. Kim, Y.J. Kwon, H. Choi, J.K. Park, Y.K. Jeong, *Applied Surface Science*, 509 (2020) 144821.
50. R. Artzi-Gerlitz, K.D. Benkstein, D.L. Lahr, J.L. Hertz, C.B. Montgomery, J.E. Bonevich, S. Semancik, M.J. Tarlov, *Sensors and Actuators B: Chemical*, 136 (2009) 257–264.
51. M. Drobek, J.-H. Kim, M. Bechelany, C. Vallicari, A. Julbe, S.S. Kim, *ACS Appl. Mater. Interfaces*, 8 (2016) 8323–8328.
52. M. Weber, J.-H. Kim, J.-H. Lee, J.-Y. Kim, I. Iatsunskyi, E. Coy, M. Drobek, A. Julbe, M. Bechelany, S.S. Kim, *ACS Appl. Mater. Interfaces*, 10 (2018) 34765–34773.
53. J. Jae, G.A. Tompsett, A.J. Foster, K.D. Hammond, S.M. Auerbach, R.F. Lobo, G.W. Huber, *Journal of Catalysis*, 279 (2011) 257–268.
54. J. Wilcox, Carbon Capture, Springer New York, (2012) New York, NY, pp. 245–255.
55. W. Xiao, D.Y. Hui, C. Zheng, D. Yu, Y.Y. Qiang, C. Ping, C.L. Xiang, Z. Yi, *Nanoscale Research Letters*, 10 (2015) 130.
56. B. Gong, J.C. Spagnola, G.N. Parsons, *Journal of Vacuum Science & Technology A*, 30 (2011) 01A156.
57. A. Mavrič, M. Valant, C. Cui, Z.M. Wang, *Journal of Non-Crystalline Solids*, 521 (2019) 119493.
58. B. Pintault, A. Ayral, *Journal of Porous Materials*, 16 (2009) 73–79.
59. M. Hu, W. Kang, B. Cheng, Z. Li, Y. Zhao, L. Li, *Microchimica Acta*, 183 (2016) 1713–1720.
60. Z. Liu, X. Yang, J. Sun, F. Ma, *Materials Letters*, 212 (2018) 283–286.
61. B.-Y. Song, M. Zhang, Y. Teng, X.-F. Zhang, Z.-P. Deng, L.-H. Huo, S. Gao, *Sensors and Actuators B: Chemical*, 307 (2020) 127662.
62. P.M. Bulemo, H.-J. Cho, N.-H. Kim, I.-D. Kim, *ACS Appl. Mater. Interfaces*, 9 (2017) 26304–26313.
63. K.-I. Choi, H.-J. Kim, Y.C. Kang, J.-H. Lee, *Sensors and Actuators B: Chemical*, 194 (2014) 371–376.